

Kinetic Monte Carlo simulation framework for chemical short-range order formation kinetics in a multi-principal-element alloy



Zeqi Shen ^{a,*}, Jun-Ping Du ^{a,b,*}, Shuhei Shinzato ^a, Yuji Sato ^c, Peijun Yu ^a, Shigenobu Ogata ^{a,b,*}

^a Department of Mechanical Science and Bioengineering, Osaka University, Osaka 560-8531, Japan

^b Center for Elements Strategy Initiative for Structural Materials, Kyoto University, Kyoto 606-8501, Japan

^c Department of Mechanical Engineering, The University of Tokyo, Tokyo 113-8656, Japan

ARTICLE INFO

Keywords:

Multi-principal-element alloys
Chemical short-range order
Time-Temperature-CSRO degree diagram
Kinetic Monte Carlo

ABSTRACT

Multi-principal-element alloys—so-called high-entropy alloys (HEAs)—contain multiple equiatomic or nearly equiatomic elements and are attracting increasing attention in basic and applied research because of their superior mechanical properties. Recently, the existence of chemical short-range order (CSRO)/local chemical ordering in HEAs has been experimentally confirmed and its effects on the mechanical properties of HEAs have been studied. However, the formation process and kinetics of CSRO have not yet been fully clarified. In the present study, we propose a simulation framework to study CSRO formation kinetics based on Monte Carlo and kinetic Monte Carlo simulation methods. Applying the simulation framework to quinary face-centered-cubic multi-principal-element alloys described by Lennard-Jones interatomic model potentials, we obtained the temperature-dependent CSRO formation kinetics via vacancy diffusion and constructed a time–temperature–CSRO degree diagram, which enables the CSRO of HEAs to be tailored via thermal processing.

1. Introduction

Multi-principal-element alloys, also known as high-entropy alloys (HEAs) [1–7], contain multiple equiatomic and nearly equiatomic elements but with a chemically random atomic arrangement in their on-lattice configuration. HEAs have attracted the interest of materials scientists and engineers because of their unique and excellent mechanical properties [8], such as high strength and hardness. Compared with conventional alloys, HEAs also exhibit superior resistance to oxidation [9], corrosion [10,11], fatigue [12,13], fracture [3] and irradiation [14] by adjusting compositions. Based on the assumption that HEAs are random single-phase solid solutions, its improved properties are attributed to the unique characteristics it has [15], namely high mixing entropy, severe lattice distortion, sluggish diffusion and cocktail effect. The four characteristics has been successfully applied to explain the superior properties of HEAs exhibited in experiments.

Recent, experimental and theoretical studies have shown that the on-lattice atomic chemical arrangement is not entirely random [16–23]. HEAs are composed of atoms of various elements and thus have multiple interatomic interactions. This variety of interactions can lead to a chemically ordered atomic arrangement, which is known as chemical

short-range order (CSRO) or local chemical ordering [18–22]. Because CSRO affects the mechanical properties of HEAs [17,21–24], controlling the occurrence of CSRO enables tailoring of the mechanical properties of HEAs. The CSRO may occur from the chemically random atomic arrangement during quenching from the melt state or as a result of annealing at a certain temperature. The time and temperature necessary to form CSRO is specified by a time–temperature–CSRO degree (TTC) diagram. To the best of our knowledge, not only the TTC of HEAs but also a predicting framework for the TTC have not yet been reported.

In the present study, we propose a simulation framework to obtain the TTC diagram corresponding to CSRO formation in HEAs based on kinetic Monte Carlo (kMC) simulations under the assumption that vacancy diffusion dominates the CSRO formation kinetics.

2. Methods

2.1. Kinetic Monte Carlo simulation and Monte Carlo simulation methods

We used the kMC method to model the vacancy diffusion kinetics in HEA [25]. The event of a vacancy jumping to a neighboring atomic site, such as one of the twelve nearest-neighbor sites in the face-centered

* Corresponding authors at: Center for Elements Strategy Initiative for Structural Materials, Kyoto University, Kyoto 606-8501, Japan (J.-P. Du); Department of Mechanical Science and Bioengineering, Osaka University, Osaka 560-8531, Japan (S. Ogata).

E-mail addresses: zeqi.shen@tsme.me.es.osaka-u.ac.jp (Z. Shen), j pdu@tsme.me.es.osaka-u.ac.jp (J.-P. Du), ogata@me.es.osaka-u.ac.jp (S. Ogata).

cubic (FCC) structure, was taken as the kMC event. The frequency of the vacancy jump was estimated using the Arrhenius equation; thus, the jump rate k_I of a vacancy to a neighboring site I was computed by

$$k_I = \nu_0 \exp\left(-\frac{\Delta E}{k_B T}\right) \quad (1)$$

where T is temperature, $\nu_0 = 10^{13} \text{ s}^{-1}$ is a trial frequency (here simply taken as the typical vibrational frequency of an atom in the crystal), ΔE is the energy barrier of the vacancy–atom exchange calculated on-the-fly during the kMC simulation using the nudged elastic band (NEB) method [26], and k_B is the Boltzmann constant. Here we assumed that the effect of the activation entropy (of the order of k_B) on the diffusion free energy barrier is negligible in the vacancy diffusion process. The incubation time of the vacancy jump was computed as [25]

$$t = -\frac{1}{k_{\text{sum}} \ln(s)} \quad (2)$$

where $k_{\text{sum}} = \sum_{I=1}^n k_I$, n is the number of neighboring sites of the vacancy, and s is a random number between 0 and 1. The atomic structure was fully relaxed by the conjugate gradient method at every kMC step before NEB energy barrier analysis was performed.

Monte Carlo (MC) simulation was used to compute the temperature-dependent degree of CSRO at a thermal equilibrium state at each temperature. A direct atom exchange between two randomly selected atoms in the FCC HEA atomic model was taken as the MC event [19,22]. The atomic structure was fully relaxed by the conjugate gradient method at every MC step, thereby relaxing the atomic position both before and after the atom-exchange MC step. In the same MC method, an atom exchange was always accepted when the energy after the exchange decreased; by contrast, when the energy after the exchange increased, the atom exchange was accepted with the acceptance probability of $\exp(-\Delta\tilde{E}/(k_B T))$, where $\Delta\tilde{E}$ is the change in energy resulting from the atom exchange.

2.2. CSRO parameter

To quantitatively describe the degree of CSRO for a given FCC on-lattice atomic arrangement, we defined the CSRO parameter [23,27]:

$$\alpha_{\alpha\beta}^m = \frac{P_{\alpha\beta}^m - C_\beta}{\delta_{\alpha\beta} - C_\beta} \quad (3)$$

where m is the m -th nearest-neighbor shell of the central atom α , C_β is the average concentration of element β in the bulk HEA, and $P_{\alpha\beta}^m$ is the appearance probability of element β around element α in the m -th nearest-neighbor sites of the atom of element α . Parameter $\delta_{\alpha\beta}$ is the Kronecker delta function; if α is the same as β , then $\delta_{\alpha\beta}$ is equal to 1, otherwise $\delta_{\alpha\beta}$ is equal to 0. The CSRO parameter is closer to 0 when the atomic arrangement is more random (disordered). For the pair of atoms of the same elements ($\alpha = \beta$), a positive $\alpha_{\alpha\beta}^m$ denotes the attractive tendency for the atoms, and a negative $\alpha_{\alpha\beta}^m$ denotes the opposite. For the pair of atoms of different elements ($\alpha \neq \beta$), a positive $\alpha_{\alpha\beta}^m$ denotes the repulsive tendency for the atoms, and a negative $\alpha_{\alpha\beta}^m$ denotes the opposite. In the present study, because we study quinary HEA, as described later, there are fifteen different CSRO parameters.

2.3. Model interatomic interaction and CSRO thermodynamic properties

A 12–6-type, simple Lennard–Jones (LJ) model potential [28] was used to describe the atomic interactions in a quinary HEA model:

$$V_{\text{LJ}}^{\alpha\beta} = 4\epsilon_{\alpha\beta} \left\{ \left(\frac{\sigma_{\alpha\beta}}{r}\right)^{12} - \left(\frac{\sigma_{\alpha\beta}}{r}\right)^6 \right\} \quad (4)$$

where $\epsilon_{\alpha\beta}$ is the depth of the potential well, $\sigma_{\alpha\beta}$ is the distance beyond

Table 1

LJ potential parameters for a HEA [28].

Parameter	Value (eV)	Parameter	Value (Å)
ϵ_{11}	0.400	σ_{11}	2.336
ϵ_{22}	0.500	σ_{22}	2.284
ϵ_{33}	0.500	σ_{33}	2.319
ϵ_{44}	0.400	σ_{44}	2.440
ϵ_{55}	0.500	σ_{55}	2.281

which the potential energy becomes negative, and α and β are chemical species of atoms. To investigate CSRO thermodynamics and kinetics, we designed two LJ potentials: one potential demonstrates almost no thermodynamic driving force of CSRO formation, and the other describes a strong thermodynamic driving force of CSRO formation and phase separation. The parameters describing interactions between atoms of the same element were referred from the work of Zhen and Davies [28] for both LJ potentials (see Table 1). We used parameters for Cr, Co, Fe, V, and Ni. The cross parameters between different chemical species were defined by the simple geometric mean in the former no-driving-force LJ: $\epsilon_{\alpha\beta} = \sqrt{\epsilon_{\alpha\alpha}\epsilon_{\beta\beta}}$, $\sigma_{\alpha\beta} = \sqrt{\sigma_{\alpha\alpha}\sigma_{\beta\beta}}$ (original LJ). Note that, here we modified the parameter $\epsilon_{\alpha\alpha}$ from the literature [20] to realize a model thermodynamics, in which CSRO-free structure is stable regardless of annealing temperature without the following cross parameter modification. Meanwhile, in the latter strong-driving-force LJ (modified LJ), to demonstrate the CSRO formation trend, the cross parameters between elements 1 and 2 were modified to $\epsilon_{12} = 0.600$, $\sigma_{12} = 2.310$ (modified LJ) from the original LJ, which models the strong interaction between specific elements in actual HEAs, for example, Ni-Al and Fe-Si interactions in FeCoNi(AlSi)_x HEA [20] and Co-Cr interaction in NiCoCr MEA [23]. In the latter literature, CSRO formation and phase separation have been actually demonstrated by MC annealing simulation using more realistic embedded atom method potential.

Before studying the CSRO formation process, we investigated the temperature-dependent CSRO degree in a thermodynamic equilibrium state at each temperature because the equilibrium state is the final destination and can thus serve as a reference state for simulating vacancy-diffusion-driven kMC CSRO formation, as we discuss later. An atom-exchange MC simulation was performed to achieve the equilibrium state at each temperature, where the equilibrium state was defined as a maximum potential energy variation per atom of $3 \times 10^{-3} \text{ eV/atom}$ or less within the last 100,000 MC steps. We used an atomic model composed of $9 \times 9 \times 9$ FCC units with 2916 atoms, and the average lattice constants were 3.60 \AA for quinary alloys in both the original LJ and the modified LJ systems.

Fig. 1(a) and (b) shows the temperature-dependent CSRO degree at the equilibrium state, as obtained using the MC simulations. The horizontal axis is the homologous temperature normalized by the melting point. The melting points of these systems were $T_m = 0.65\epsilon_{\text{ave}}/k_B$ for the original LJ and $T_m = 0.67\epsilon_{\text{ave}}/k_B$ for the modified LJ, where $\epsilon_{\text{ave}} = \sum_{i=1}^5 \epsilon_{ii}/5$. The melting points were determined by direct MD simulation of liquid–solid boundary migration in a two-phase model, as described in the [Supplementary Information](#). The vertical axis in Fig. 1(a) and (b) is the CSRO parameter. In Fig. 1(a) and (b), the quinary model HEA with the original LJ demonstrates almost no chemical ordering irrespective of temperature; by contrast, the model with the modified LJ demonstrates strong chemical ordering, as evidenced by the large finite values of the CSRO parameters. The degree of CSRO increases with decreasing temperature, and the chemical ordering appears to exist to a certain degree even at the melting point in the quinary model HEA with the modified LJ.

The potential energy changes in the MC simulations are shown in Fig. 1(c) and (d). The results indicate that the chemical ordering induces a reduction of potential energy (enthalpy). Parameter α_{12}^1 in Fig. 1(b)

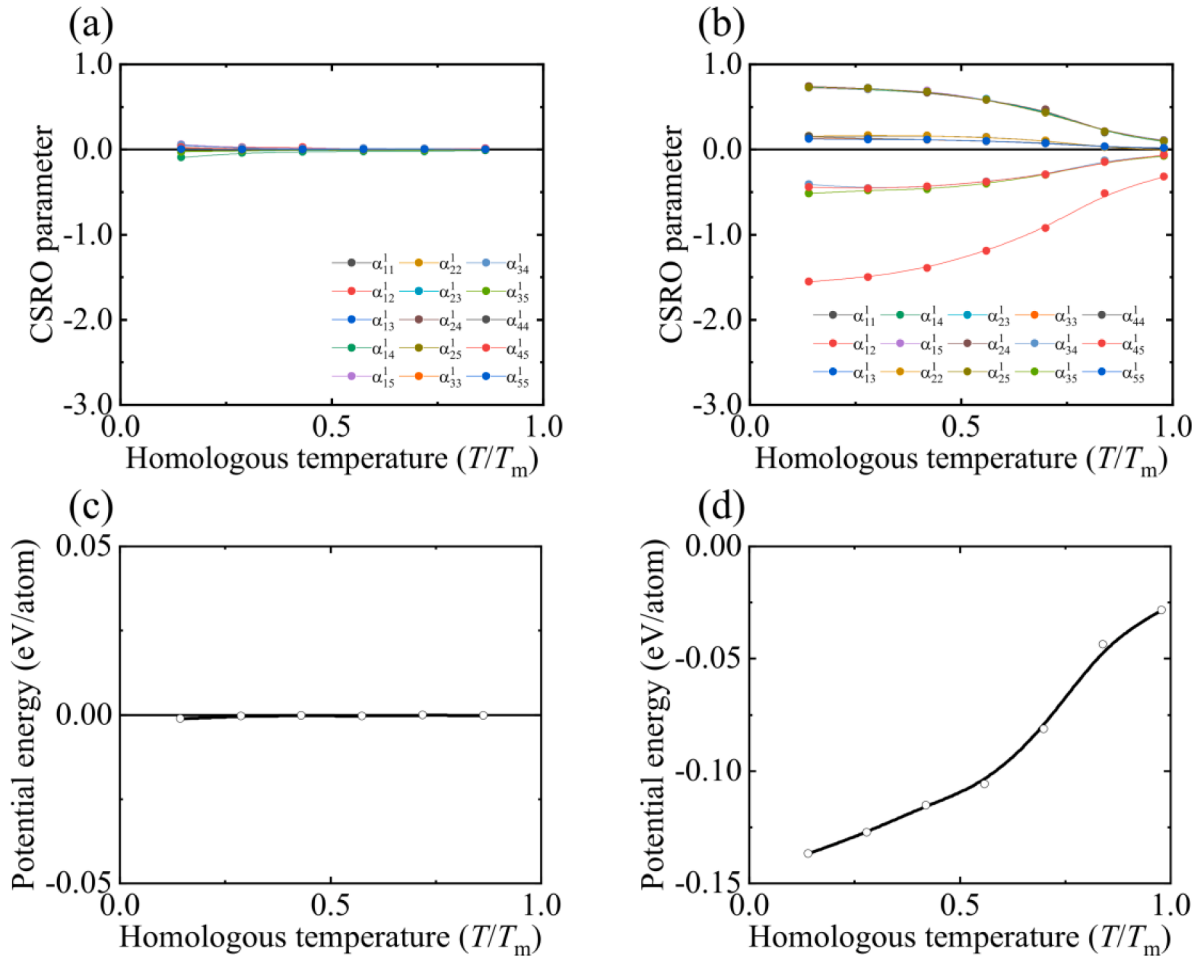


Fig. 1. The temperature dependence of CSRO: (a) original LJ and (b) modified LJ. Potential energy of the equilibrium state reached by MC simulation with (c) the original LJ (Table I) and (d) the modified LJ. The energy reference of (c) and (d) is taken as the energy of random configuration ($\alpha_{\alpha\beta}^m = 0$).

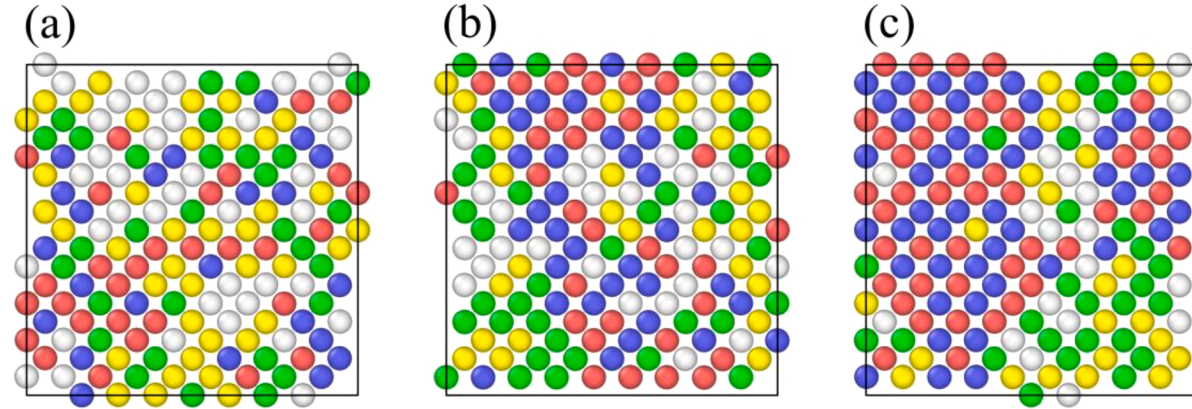


Fig. 2. Equilibrium structure of the quinary model HEA (modified LJ) at different temperatures: (a) $0.97T_m$, (b) $0.83T_m$, and (c) $0.42T_m$. The balls denote atoms colored by their types of elements.

exhibits the largest negative value among the fifteen CSRO parameters for the HEA, reflecting that the atomic interaction between elements 1 and 2 in the quinary HEA (modified LJ) is the strongest among the interatomic interactions in these alloys. Notably, at temperatures lower than $\sim 0.9T_m$ in the quinary HEA, clear phase separation occurs, with a large negative value of the CSRO parameter, as evident in the temperature-dependent equilibrium structure shown in Fig. 2. These results suggest that a very long annealing time at lower temperatures

may eventually lead to phase separation instead of CSRO formation. Such phase separation has been well observed in experiments with HEAs [29]. Thus, the TTC provides important information for the design of a thermal protocol for attaining CSRO without such phase separation. Notably, in the following discussions, only the α_{12}^1 CSRO parameter among the fifteen parameters in Fig. 1(b) is used to representatively indicate the degree of ordering.

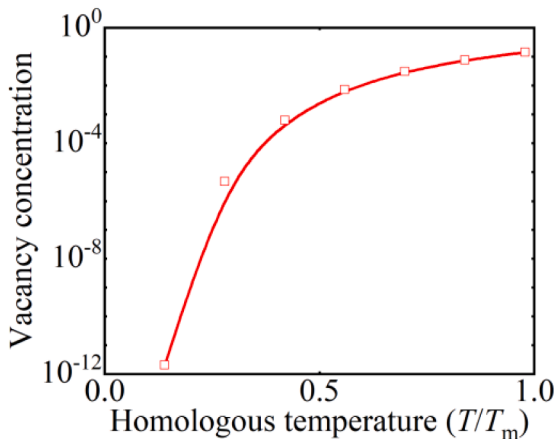


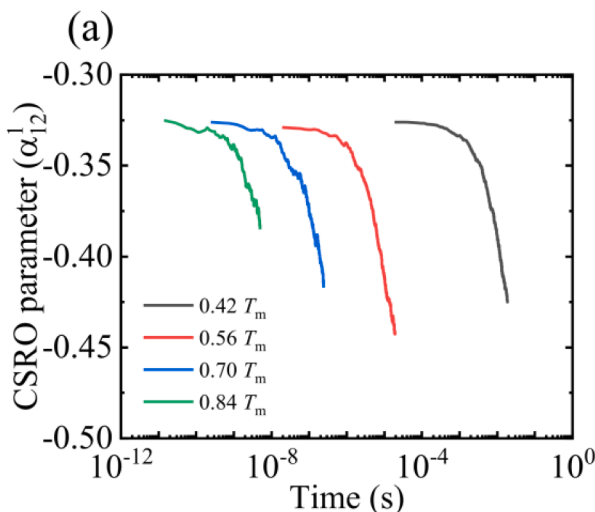
Fig. 3. Equilibrium vacancy concentration at different temperatures.

3. Kinetics of chemical short-range ordering

The time and temperature dependences of the CSRO formation kinetics were analyzed using the kMC method. Again, vacancy diffusion was assumed to be the fundamental mechanism of CSRO formation through the shuffling of the chemical (atomic) arrangement in the FCC lattice. The same $9 \times 9 \times 9$ FCC atomic model as that used in the MC analyses but with one vacancy, such as 2916 FCC sites with 2915 atoms + one vacancy, was used in the subsequent kMC analyses. The equilibrium structure (atomic arrangement) obtained by MC annealing simulation at melting point was chosen as the initial structure (atomic arrangement) with CSRO degree of $\alpha_{12}^1 = -0.32$.

Since the vacancy concentration directly affects the formation time of CSRO by increasing the average vacancy jump frequency in the unit volume of the system, actual vacancy concentration must be estimated and the obtained timescale using the atomic model should be modified by the ratio of vacancy concentration of actual and model systems. The equilibrium dilute vacancy concentration (number density) in the multicomponent system at different temperatures was approximately computed by [30]

$$x_v = \frac{\exp\left(n - 1 - \frac{u}{k_B T}\right)}{n + \exp\left(n - 1 - \frac{u}{k_B T}\right)} \quad (5)$$



where n is the number of components and u is an average of the vacancy formation energies of different atomic sites. The vacancy formation energy calculated with the LJ potential is known to always be nearly equal to the cohesive energy [31], which is much higher than the actual vacancy formation energy. This discrepancy is an intrinsic shortcoming of pair potential and contradicts the experimental results [32]. Theoretical calculations [32] have indicated that the vacancy formation energy can be approximately computed as one-third of the cohesive energy,

$$u \approx E_{\text{cohesive}}/3 \quad (6)$$

Fig. 3 shows the temperature-dependent vacancy concentration computed using Eq. (5). The cohesive energy in Eq.(6) was taken as the average cohesive energy of fully random HEA model. The actual time in the kinetic of CSRO formation in the following discussions was estimated on the basis of a timescale conversion using the kMC simulation time t^{kMC} , such as $t = t^{\text{kMC}} \times x_v^{\text{kMC}}/x_v$, under the assumption that the diffusivity is nearly proportional to the vacancy concentration, where $x_v^{\text{kMC}} = 1/2916 = 3.43 \times 10^{-4}$ is the vacancy concentration of the atomic model used in the kMC simulation.

Fig. 4 shows the time evolutions of the CSRO parameter and potential energy at different temperatures during the kMC simulations. The time was again previously converted to the actual time using the aforementioned method. The horizontal broken lines in Fig. 4(b) represent the potential energy at the equilibrium state at each temperature, as computed in the MC simulations (Fig. 1(d)). Each plot was derived by taking an average of seven simulations using chemical structures with different initial randomness.

To more clearly present the energetics of the vacancy jump process, we analyzed the distribution (histogram) of potential energy difference between before and after kMC jump (ΔE_1) and potential energy barrier of forwarding jump (ΔE_2) (see Fig. 5) for the accepted jump during the kMC simulation. Since the distribution should be continuously changed during the kMC simulation due to the vacancy-migration-induced atomic-structure-change (quenching induced CSRO change), we estimated the distribution at two stages in the kMC simulations, such as the early stage and the subsequent stage (at different CSRO levels), for the two temperatures ($0.56T_m$, $0.84T_m$) for each LJ potentials (original and modified LJs). For both the original and modified LJs, the ranges of ΔE_1 and ΔE_2 are ~ 1 eV ($= 3.87k_B T$ at $0.84T_m$), which is not far from the values presented in the literature using more realistic interatomic potential ($3.60k_B T$ at 500 K) [33]. We observed no obvious differences between the distributions at the early and subsequent stages in the kMC

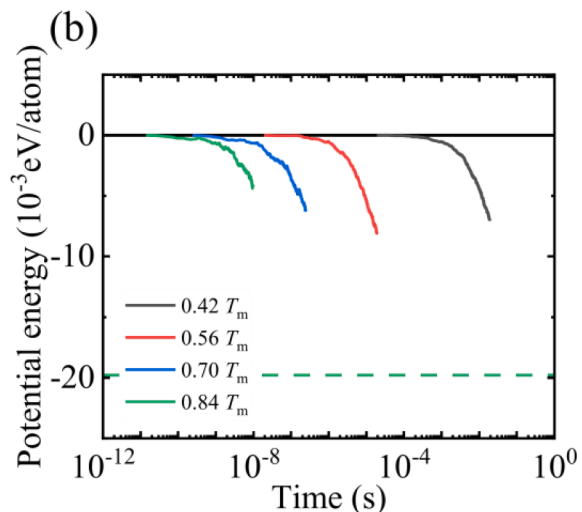


Fig. 4. The time evolutions of the CSRO parameter and the potential energy for the quinary model HEA (modified LJ): (a) CSRO parameter (α_{12}^1) and (b) potential energy. The horizontal broken lines show the potential energy under equilibrium conditions computed in the MC simulation (see Fig. 1(d)).

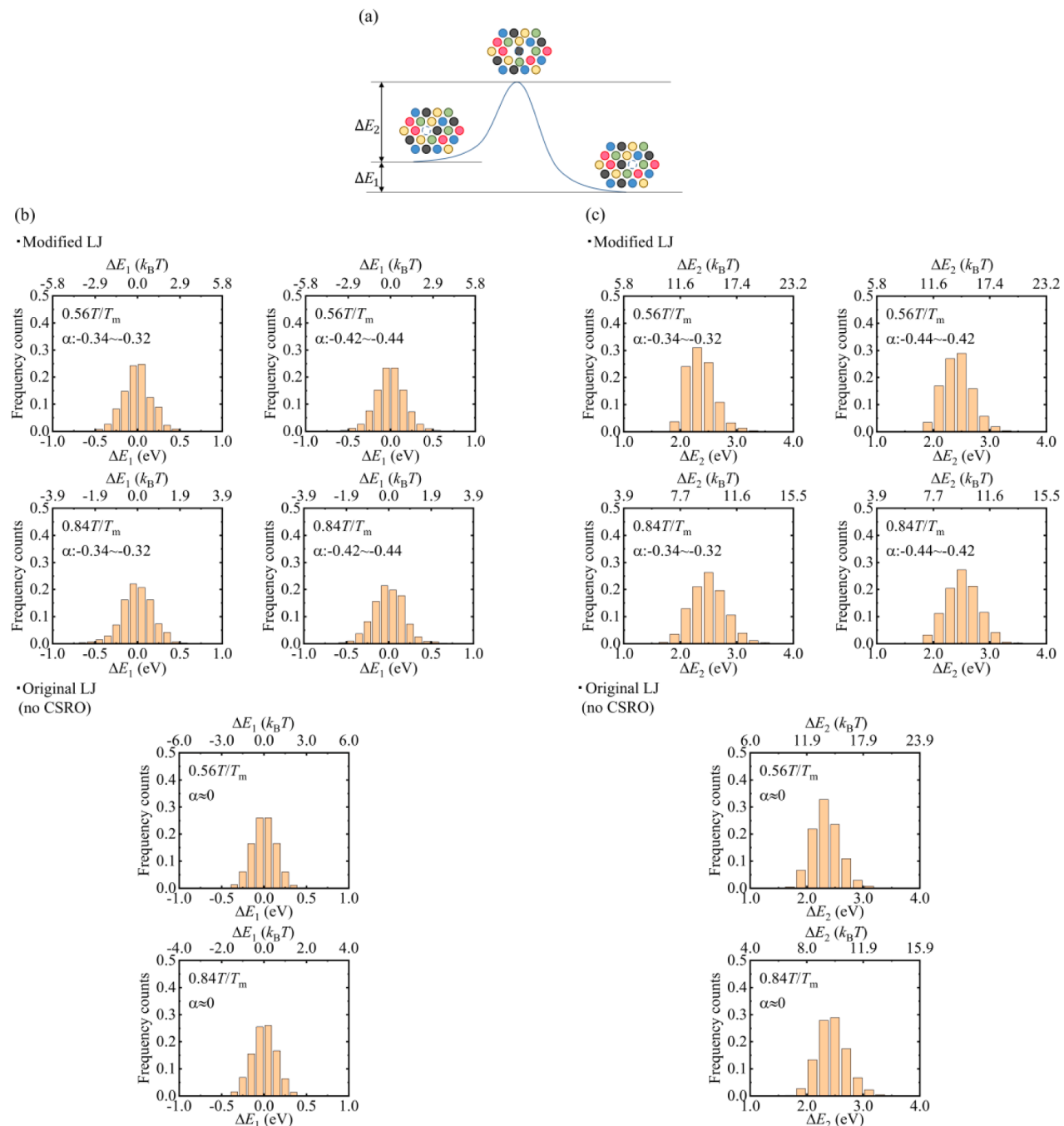


Fig. 5. Potential energy barrier distributions (histogram) for vacancy jump along vacancy diffusion pathway at $T = 0.56T_m$ and $0.84T_m$ at different CSRO levels α ($= \alpha_{12}^1$) using original LJ and modified LJ. (a) definition of energies ΔE_1 (potential energy change between initial and final states of vacancy jump) and ΔE_2 (potential energy barrier of vacancy jump), (b) distribution of ΔE_1 , and (c) distribution of ΔE_2 .

simulations using the original LJ regardless of simulation temperature because of no CSRO formation at any temperatures. More importantly, in the kMC simulations using the modified LJ, we can find that after certain CSRO formation (at larger α_{12}^1) both ΔE_1 and ΔE_2 distributions slightly shift toward the higher energy side. Thus, CSRO formation increases the energy barrier of vacancy diffusion along the vacancy diffusion pathway.

Notably, because of limited computational time, the kMC simulations were terminated before reaching the equilibrium state, as evident in Fig. 4(b); thus, these results correspond to a nonequilibrium CSRO state. To extend the kMC results and predict the whole process from the random state to the thermal equilibrium state, we used an empirical

time-dependent relaxation function [34] to predict the time evolution of the CSRO parameter:

$$\frac{\alpha(t)}{\alpha_{\text{equ}}} = 1 - e^{-f_1(T)(t+f_2(T))^a} \quad (7)$$

where t is the time necessary to achieve a CSRO degree of α ($= \alpha_{12}^1$), T is the formation temperature, time exponent a is a parameter, and α_{eq} is the CSRO parameter α_{12}^1 at the equilibrium state, as calculated by MC simulation (Fig. 1(b)). Here, $f_1(T)$ and $f_2(T)$ was a quadratic polynomial function of T in units of s^{-a} and s .

We fitted the function to the data ranging from $0.42T_m$ to $0.98T_m$, as calculated by the kMC, and the coefficient of determination of the fitting

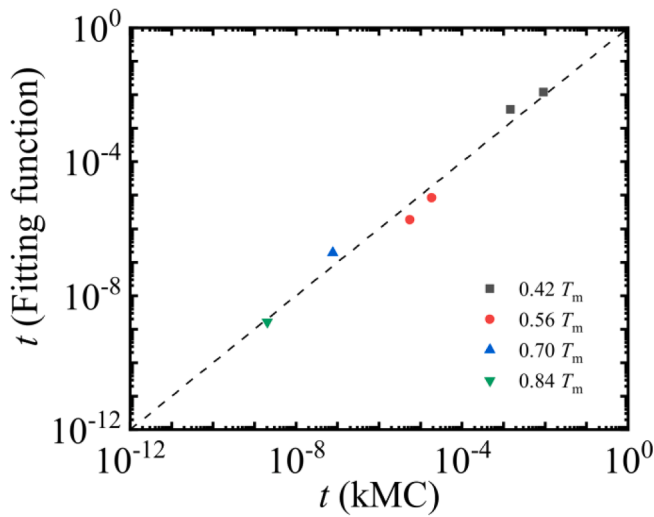


Fig. 6. Comparison of the formation time necessary to obtain CSRO with $\alpha_{12}^1 = -0.35$ and -0.40 at different temperatures, as obtained by a fitting function (Eq. (11)) and from actual kMC data.

is $R^2 = 0.65$. Then, we obtained the following equations:

$$\frac{\alpha(t)}{\alpha_{\text{equ}}} = 1 - e^{-f_1(T)(t+f_2(T))^0.7} \quad (8)$$

$$\log(f_1(T)) = -6.88 \times 10^{-7}T^2 + 0.00646T - 7.62117 \quad (9)$$

$$\log(f_2(T)) = 1.34 \times 10^{-6}T^2 - 0.01031T - 10.91606 \quad (10)$$

Thus,

$$t = \sqrt[0.7]{-\frac{1}{f_1(T)} \ln \left(1 - \frac{\alpha}{\alpha_{\text{equ}}} \right)} - f_2(T) \quad (11)$$

Fig. 6 shows a comparison between the function in Eq. (11) and actual kMC data for the formation time of CSRO with $\alpha_{12}^1 = -0.35$, and -0.40 . The formation time predicted by the fitting function well

reproduces the kMC results.

Using the fitting function and Eq. (11), we eventually computed the TTC curve (Fig. 7). The solid line in Fig. 7 represents the results calculated by the fitting function, and the dots represent the data obtained by the kMC calculation. The TTC curve indicates the annealing time and temperature ranges/quenching rate range necessary to attain a certain degree of CSRO without inducing phase separation. When quenching is carried out from a melt, an excessively high quenching rate (e.g., $\dot{T}/T_m > 10^9 \text{ s}^{-1}$) should result in an almost random structure (but still with a certain level of CSRO as seen in Fig. 1(b)); by contrast, an excessively low quenching rate (e.g., $\dot{T}/T_m < 10^3 \text{ s}^{-1}$) lead to phase separation as we discuss later. Thus, in this model HEA, quenching rates within $10^9 \text{ s}^{-1} > \dot{T}/T_m > 10^3 \text{ s}^{-1}$ may lead to a certain CSRO without phase separation. Notably, it can be expected that an excessively high quenching rate may lead to a noncrystalline or glass/amorphous structure.

There are both the CSRO structure and separated phase ordering in the equilibrium structure using modified LJ below $\sim 0.9T_m$, while at the temperature close to the T_m the equilibrium structure does not show clear phase separation, and is thus almost like “pure” CSRO structure as shown in Fig. 2. The same trend can be seen also in the literature using more realistic embedded atom method potentials for CoCrNi [23]. To more quantitatively demonstrate the phase separation, we would propose the following algorithm to distinguish the phases. First, by computing chemical composition in a region surrounding an atom (within 7 Å sphere centered at the atom), we specified which phase the atom belongs. By carefully observing atomic arrangement after phase separation happens (Fig. 2), we found three characteristic phases, such as (i) phase having much greater number of atoms 1 and 2 than the average chemical composition (phase 1), (ii) phase having a much smaller number of atoms 1 and 2 than the average chemical composition, (iii) phase in-between them having similar number of atoms 1 and 2 to the average chemical composition. In practice, we distinguished three phases as follows: if $C_1 + C_2 > 0.7 \rightarrow$ phase 1, if $C_1 + C_2 < 0.2 \rightarrow$ phase 2, the others \rightarrow phase 3, where $C_i = N_i/N$, N_i is a number of element- i in the sphere, and N is a total number of atoms in the sphere. Then, we applied this algorithm for all the atoms in the model and compute the volume fraction (atom-number fraction) of each phase and

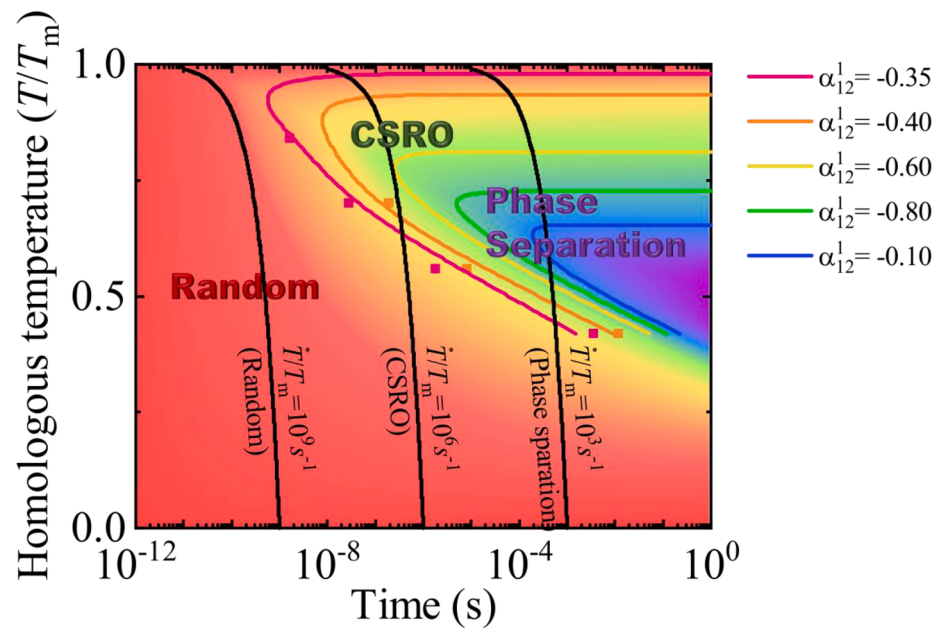


Fig. 7. Time-temperature-CSRO degree (TTC) diagram for the quinary model HEA, as calculated using a fitting function with a modified LJ potential. Dots indicate data directly obtained by kMC. Larger α_{12}^1 values imply phase separation, as discussed in the text. The solid black lines show temperature changes at constant

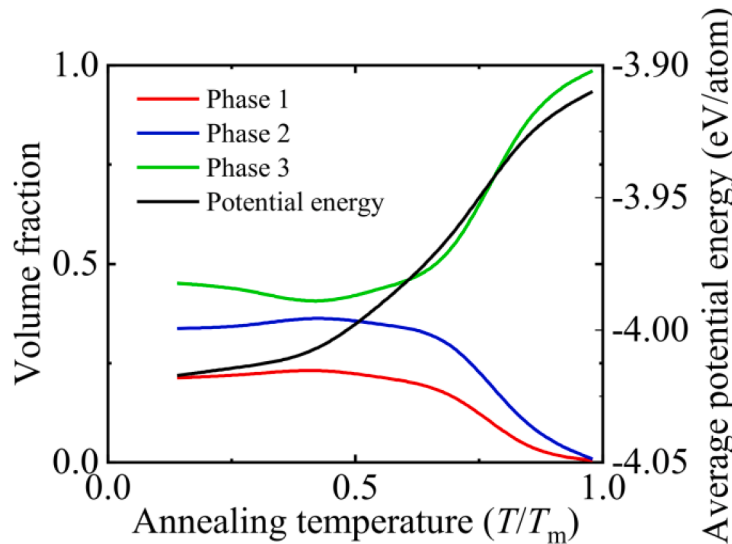


Fig. 8. Annealing temperature-dependent volume fraction (atom number fraction) of each phase and average potential energy of whole system.

presented in Fig. 8. Fig. 8 clearly captures the trend of phase separation with respect to annealing temperature.

Moreover, to examine phase stability at low temperatures, we compute average potential energies of the phase-separated structures at well-below T_m and the almost pure CSRO structure annealed at just below T_m . The former structures' potential energy is -3.90 eV/atom, and the latter structures' potential energy is -4.02 eV/atom as shown in Fig. 8, demonstrating that there is always a driving force to the phase separation due to the potential energy difference. Thus, at lower temperatures, the phase separation can occur because the driving force due to the potential energy difference is dominant. In contrast, at higher temperatures, the phase separation becomes hard to happen because a more random (but still with certain CSRO) structure becomes more stable due to the configurational entropic effect. The CSRO structure must have higher configurational entropy than the phase-separated structure; thus, the thermodynamic driving force to the phase separation becomes weaker and maybe negative at higher temperatures.

4. Conclusions

A simulation framework was proposed to obtain a TTC diagram for a HEA based on a kMC simulation of vacancy diffusion in a HEA. The simulation framework was demonstrated using the LJ model potential for quinary alloys. The TTC curve indicates the annealing time and temperature ranges/quenching rate range necessary to attain a certain degree of CSRO without phase separation. Although the assumption of random solid solution has been successfully applied to explain the superior properties of HEAs compared to conventional alloys, it has been experimentally shown that HEAs deviate from random solid solution to form CSROs during thermal treatment [17,19,35]. And the degree of CSRO can be a key structural parameter to tuning and optimizing the mechanical properties of HEAs [36]. The experimental measurement of CSRO and observation its formation mechanism are time-consuming, which makes it very challenging to determine the relationship between CSRO degree, annealing time and annealing temperature in experiments. Our simulation framework provides a useful reference for the establishment of such time-temperature-CSRO degree diagrams in experiments. Although we need to employ more realistic interatomic interactions for a specific HEA to discuss the results quantitatively, the proposed simulation framework can be generally applied to any HEAs.

5. Data availability

The data that support the findings of this study are available from the corresponding author upon reasonable request.

CRediT authorship contribution statement

Zeqi Shen: Methodology, Software, Writing - original draft. **Jun-Ping Du:** Methodology, Software, Formal analysis, Writing - original draft. **Shuhei Shinzato:** Methodology, Software. **Yuji Sato:** Methodology, Software. **Peijun Yu:** Methodology, Software. **Shigenobu Ogata:** Conceptualization, Writing - original draft, Supervision, Project administration.

Declaration of Competing Interest

The authors declare that they have no known competing financial interests or personal relationships that could have appeared to influence the work reported in this paper.

Acknowledgements

This work was supported by Element Strategy Initiative for Structural Materials of MEXT, Grant Number JPMXP0112101000. P.Y and S.O. acknowledge the support by the JSPS KAKENHI Grant Nos. JP18H05450 and JP18H05453, S.O. acknowledges the support by the JSPS KAKENHI Grant Nos. JP17H01238 and JP17K18827. S.S. acknowledges the support by the JSPS KAKENHI Grant No. JP19K23487.

Appendix A. Supplementary data

Supplementary data to this article can be found online at <https://doi.org/10.1016/j.commatsci.2021.110670>.

References

- [1] F. Otto, A. Dlouhý, C.h. Somsen, H. Bei, G. Eggeler, E.P. George, The influences of temperature and microstructure on the tensile properties of a CoCrFeMnNi high-entropy alloy, *Acta Materialia* 61 (15) (2013) 5743–5755.
- [2] K.-Y. Tsai, M.-H. Tsai, J.-W. Yeh, Sluggish diffusion in Co–Cr–Fe–Mn–Ni high-entropy alloys, *Acta Materialia* 61 (13) (2013) 4887–4897.
- [3] B. Gludovatz, A. Hohenwarter, D. Catoor, E.H. Chang, E.P. George, R.O. Ritchie, A fracture-resistant high-entropy alloy for cryogenic applications, *Science* 345 (6201) (2014) 1153–1158.
- [4] B. Schuh, F. Mendez-Martin, B. Völker, E.P. George, H. Clemens, R. Pippan, A. Hohenwarter, Mechanical properties, microstructure and thermal stability of a

- nanocrystalline CoCrFeMnNi high-entropy alloy after severe plastic deformation, *Acta Materialia* 96 (2015) 258–268.
- [5] E.J. Pickering, R. Muñoz-Moreno, H.J. Stone, N.G. Jones, Precipitation in the equiatomic high-entropy alloy CrMnFeCoNi, *Scripta Materialia* 113 (2016) 106–109.
- [6] Z. Li, K.G. Pradeep, Y. Deng, D. Raabe, C.C. Tasan, Metastable high-entropy dual-phase alloys overcome the strength–ductility trade-off, *Nature* 534 (7606) (2016) 227–230.
- [7] S. Chen, H.S. Oh, B. Gludovatz, S.J. Kim, E.S. Park, Z. Zhang, R.O. Ritchie, Q. Yu, Real-time observations of TRIP-induced ultrahigh strain hardening in a dual-phase CrMnFeCoNi high-entropy alloy, *Nature Communications* 11 (1) (2020) 1–8.
- [8] E.P. George, W.A. Curtin, C.C. Tasan, High entropy alloys: A focused review of mechanical properties and deformation mechanisms, *Acta Materialia* 188 (2020) 435–474.
- [9] Y.u. Yin, Q. Tan, Y. Zhao, Q. Sun, Z. Shi, M. Bermingham, W. Zhuang, H. Huang, M.-X. Zhang, A cost-effective Fe-rich compositionally complicated alloy with superior high-temperature oxidation resistance, *Corrosion Science* 180 (2021) 109190, <https://doi.org/10.1016/j.corsci.2020.109190>.
- [10] N. Hua, W. Wang, Q. Wang, Y. Ye, S. Lin, L. Zhang, Q. Guo, J. Brechtl, P.K. Liaw, Mechanical, corrosion, and wear properties of biomedical Ti–Zr–Nb–Ta–Mo high entropy alloys, *Journal of Alloys and Compounds* 861 (2021), 157997.
- [11] C.P. Lee, C.C. Chang, Y.Y. Chen, J.W. Yeh, H.C. Shih, Effect of the aluminium content of $\text{Al}_x\text{CrFe}_{1.5}\text{MnNi}_{0.5}$ high-entropy alloys on the corrosion behaviour in aqueous environments, *Corrosion Science* 50 (7) (2008) 2053–2060.
- [12] M.A. Hemphill, T. Yuan, G.Y. Wang, J.W. Yeh, C.W. Tsai, A. Chuang, P.K. Liaw, Fatigue behavior of $\text{Al}_{0.5}\text{CoCrCuFeNi}$ high entropy alloys, *Acta Materialia* 60 (16) (2012) 5723–5734.
- [13] T.-N. Lam, S.Y. Lee, N.-T. Tsou, H.-S. Chou, B.-H. Lai, Y.-J. Chang, R. Feng, T. Kawasaki, S. Harjo, P.K. Liaw, A.-C. Yeh, M.-J. Li, R.-F. Cai, S.-C. Lo, E.-W. Huang, Enhancement of fatigue resistance by overload-induced deformation twinning in a CoCrFeMnNi high-entropy alloy, *Acta Materialia* 201 (2020) 412–424.
- [14] O. El-Atwani, N. Li, M. Li, A. Devaraj, J.K.S. Baldwin, M.M. Schneider, D. Sobieraj, J.S. Wróbel, D. Nguyen-Manh, S.A. Maloy, E. Martinez, Outstanding radiation resistance of tungsten-based high-entropy alloys, *Science Advances* 5 (3) (2019) eaav2002, <https://doi.org/10.1126/sciadv.aav2002>.
- [15] Y. Shang, J. Brechtl, C. Psitidda, P.K. Liaw, 2021, Mechanical behavior of high-entropy alloys: A review. arXiv preprint arXiv:2102.09055.
- [16] Y. Yao, Z. Huang, P. Xie, S.D. Lacey, R.J. Jacob, H. Xie, F. Chen, A. Nie, T. Pu, M. Rehwoldt, M. Zachariah, C. Wang, R. Yassar, J. Li, L. Hu, D. Yu, Carbothermal shock synthesis of high-entropy-alloy nanoparticles, *Science* 359 (6383) (2018) 1489–1494.
- [17] R. Zhang, S. Zhao, J. Ding, Y. Chong, T. Jia, C. Ophus, M. Asta, R.O. Ritchie, A. M. Minor, Short-range order and its impact on the CrCoNi medium-entropy alloy, *Nature* 581 (7808) (2020) 283–287.
- [18] C. Niu, A.J. Zaddach, A.A. Oni, X. Sang, J.W. Hurt, J.M. LeBeau, C.C. Koch, D. L. Irving, Spin-driven ordering of Cr in the equiatomic high entropy alloy NiFeCrCo, *Applied Physics Letters* 106 (16) (2015) 161906, <https://doi.org/10.1063/1.4918996>.
- [19] F.X. Zhang, S. Zhao, K. Jin, H. Xue, G. Velisa, H. Bei, R. Huang, J.Y.P. Ko, D. C. Pagan, J.C. Neufeind, W.J. Weber, Y. Zhang, Local structure and short-range order in a NiCoCr solid solution alloy, *Physical Review Letters* 118 (20) (2017), 205501.
- [20] W. Feng, Y. Qi, S. Wang, Effects of short-range order on the magnetic and mechanical properties of $\text{FeCoNi}(\text{AlSi})_x$ high entropy alloys, *Metals* 7 (11) (2017) 482.
- [21] P. Singh, A.V. Smirnov, D.D. Johnson, Atomic short-range order and incipient long-range order in high-entropy alloys, *Physical Review B* 91 (22) (2015), 224204.
- [22] A. Fernández-Caballero, J.S. Wróbel, P.M. Mummary, D. Nguyen-Manh, Short-range order in high entropy alloys: Theoretical formulation and application to Mo–Nb–Ta–VW system, *Journal of Phase Equilibria and Diffusion* 38 (4) (2017) 391–403.
- [23] Q.J. Li, H. Sheng, E. Ma, Strengthening in multi-principal element alloys with local-chemical-order roughened dislocation pathways, *Nature Communications* 10 (1) (2019) 1–11.
- [24] S. Yin, J. Ding, M. Asta, R.O. Ritchie, Ab initio modeling of the energy landscape for screw dislocations in body-centered cubic high-entropy alloys, *npj Computational Materials* 6 (1) (2020) 1–11.
- [25] A.F. Voter, in: *NATO Science Series Radiation Effects in Solids*, Springer Netherlands, Dordrecht, 2007, pp. 1–23.
- [26] H. Jónsson, G. Mills, K.W. Jacobsen, Nudged elastic band method for finding minimum energy paths of transitions, in: *Classical and Quantum Dynamics in Condensed Phase Simulations*, World Scientific, 1998, pp. 385–404, https://doi.org/10.1142/9789812839664_0016.
- [27] D. de Fontaine, The number of independent pair-correlation functions in multicomponent systems, *Journal of Applied Crystallography* 4 (1) (1971) 15–19.
- [28] S. Zhen, G.J. Davies, Calculation of the Lennard-Jones n-m potential energy parameters for metals, *Physica Status Solidi (A)* 78 (2) (1983) 595–605.
- [29] A. Manzoni, H. Daoud, R. Völkl, U. Glatzel, N. Wanderka, Phase separation in equiatomic AlCoCrFeNi high-entropy alloy, *Ultramicroscopy* 132 (2013) 212–215.
- [30] Z. Wang, C.T. Liu, P. Dou, Thermodynamics of vacancies and clusters in high-entropy alloys, *Physical Review Materials* 1 (4) (2017), 043601.
- [31] M.S. Daw, S.M. Foiles, M.I. Baskes, The embedded-atom method: a review of theory and applications, *Materials Science Reports* 9 (7–8) (1993) 251–310.
- [32] T. Korhonen, M.J. Puska, R.M. Nieminen, Vacancy-formation energies for fcc and bcc transition metals, *Physical Review B* 51 (15) (1995) 9526–9532.
- [33] Y.N. Osetsky, L.K. Béland, A.V. Barashev, Y. Zhang, On the existence and origin of sluggish diffusion in chemically disordered concentrated alloys, *Current Opinion in Solid State and Materials Science* 22 (3) (2018) 65–74.
- [34] J.C. Phillips, Stretched exponential relaxation in molecular and electronic glasses, *Reports on Progress in Physics* 59 (9) (1996) 1133–1207.
- [35] X. Chen, Q. Wang, Z. Cheng, M. Zhu, H. Zhou, P. Jiang, L. Zhou, Q. Xue, F. Yuan, J. Zhu, X. Wu, E. Ma, Direct observation of chemical short-range order in a medium-entropy alloy, *Nature* 592 (7856) (2021) 712–716.
- [36] Y. Wu, F. Zhang, X. Yuan, H. Huang, X. Wen, Y. Wang, M. Zhang, H. Wu, X. Liu, H. Wang, S. Jiang, Z. Lu, Short-range ordering and its effects on mechanical properties of high-entropy alloys, *Journal of Materials Science & Technology* 62 (2021) 214–220.